AIMS Medical Science, 3 (1): 114-125.
DOI: 10.3934/medsci.2016.1.114
Received 6 January 2016,
Accepted 16 February 2016,
Published 25 February 2016

http://www.aimspress.com/journal/medicalScience

Research Article

Modeling an Interwoven Collimator for A 3D Endocavity Gamma Camera

Yonggang Cui [1,*], Giuseppe S. Camarda [1], Anwar Hossain [1], Ge Yang [1], Utpal N. Roy [1], Terry Lall [2], and Ralph B. James [1]

[1] Brookhaven National Laboratory, Upton, NY 11973, USA;
[2] Gamma Medical Technologies, Inc., Toronto, ON M2N 6K1, Canada

*** Correspondence:** Email: ycui@bnl.gov; Tel: +1-631-344-5351; Fax: +1-631-344-5266.

Abstract: Positron emission tomography (PET) and single-photon emission-computed tomography (SPECT) are important nuclear-medical imaging tools in diagnosing cancers and creating effective treatment plans. Commercially imaging systems are operated externally and can create 3D images of the whole body or of specific organs by rotating the gamma-ray detectors, and then employing software to reconstruct the 3D images from the multiple 2D projections at different angles of view. However, their uses in intraoperative environments or for imaging specific small organs, e.g., the prostate, ovary, and cervix, are limited because of their bulky designs and the long working-distance, hence causing low efficiency and poor spatial-resolution. In such situations, compact imaging devices, e.g., the trans-rectal gamma camera developed at Brookhaven National Laboratory (BNL) and Hybridyne Imaging Technologies, are preferable for detecting intra-prostatic tumors. The camera uses pixilated cadmium zinc telluride (CdZnTe) detectors with a matched parallel-hole collimator. However, their lack of 3D imaging capability limits their use in clinics, because the acquired images cannot be interpreted easily due to missing depth information. Given the constraint on space in such operations, the traditional 3D-image acquisition methods are impractical. For this reason, we designed an interwoven collimator dedicated for 3D imaging using an endocavity probe. This novel collimator allows us to take two or multiple views of a specific organ or tissue without rotating the camera. At the first stage of design for the collimator, we carried out Monte-Carlo simulations to study the response of the collimator and the attached detectors to gamma rays, and then developed a

maximum-likelihood-based algorithm for reconstructing 3D images. In this paper, we detail our modeling of the collimator on a cluster Linux computer, and discuss the imaging capability of this novel collimator.

Keywords: gamma camera; interwoven collimator; prostate cancer; 3D imaging; CdZnTe detector; Geant4; Monte-Carlo simulation

1. Introduction

Positron emission tomography (PET) and single-photon emission computed tomography (SPECT) are important nuclear medical imaging tools in diagnosing cancers and creating effective treatment plans [1]. Commercial imaging systems are operated externally and create 3D images of the whole body or specific organs by rotating the gamma-ray detectors, and then employing software to reconstruct the 3D images from the multiple 2D projections at different angles-of-view. Their uses in an intraoperative environment or for specific small organs, e.g., the prostate, ovary, and cervix, are limited because of their bulky designs, and the long working distance, hence causing low efficiency and poor spatial resolution. In such situations, compact imaging devices, e.g., the trans-rectal gamma camera, ProxiScan, developed at Brookhaven National Laboratory (BNL) and Hybridyne Imaging Technologies for detecting intra-prostatic tumors are preferable [2].

Prostate cancer is a very common disease. According to American Cancer Society, 1 in 7 men will develop the disease in his lifetime, and 1 in 38 will die from it [3]. Although current medical imaging techniques, such as magnetic resonance imaging (MRI), computed tomography (CT), SPECT, and PET are effective tools in diagnosing cancers, none are specific for prostate cancer because of their low specificity and sensitivity, and their poor spatial resolution [4,5]; this is especially problematic when the tumors are small, at their early stages, and are confined within the prostate gland. Currently, ultrasound-guided biopsy remains the gold standard in confirming the disease. However, ultrasound cannot pinpoint precisely the tumor’s location. It only assists physicians in defining the boundaries of the glands and regions with density variations; eventually, tissue from the glands must be taken randomly, evenly, or via ultrasound guidance; hence, small tumors very easily can be missed. New imaging techniques are in high demand by patients and physicians. Ideally, such techniques should have high sensitivity and high spatial-resolution in imaging prostate cancer, and in pinpointing cancerous tumors confined with the gland, both of which would assist physicians during the tissue-extraction process for biopsies and for treatment of the disease via localized therapy. One promising option lies in devising a compact trans-rectal gamma camera that can acquire images of the prostate gland through the rectal wall. Such a short working distance greatly will also increase the sensitivity and spatial resolution.

The ProxiScan planar gamma camera was built with cadmium zinc telluride (CdZnTe) radiation detectors. CdZnTe has excellent material properties and performance for detecting gamma-rays and is attractive for applications in medical imaging. The detector modules, when fabricated in advanced pixilation and hybridization processes, can be very compact, and already are finding applications in endo-cavity measurements. ProxiScan technology has moved successfully from laboratory tests to clinical trials. However, its lack of 3D imaging capability limits its use in clinics, because the acquired images cannot be interpreted easily because of the missing depth information. Given the constraint of space during such operations, the traditional 3D image-acquisition methods involving rotation about an object of interest are impractical. To resolve this problem, we created an interwoven collimator. This innovative design allows us to image the prostate organ simultaneously from different angles of view, and extract depth information in interesting regions from the reconstructed 3D images.

In this paper, we discuss the method we used for modeling the detector and the collimator, and the algorithm that we employed for reconstructing 3D images. We show the results of simulations demonstrating the 3D imaging capability of the interwoven collimator.

2. Methods

2.1. Interwoven collimator

Figure 1a illustrates the concept of an interwoven collimator. The design is based on the traditional parallel-hole collimator, but has two modifications so to achieve 3D imaging capability: (1) All the parallel holes are slanted instead of perpendicular to the collimator's surface; and, (2) the rows of the parallel holes are separated into two groups, with one group including all the odd rows, and with all the holes facing one direction, and the other group having the even rows and with all the holes facing the second direction. One possible design is that the two slant angles of the groups are at complementary angles, as shown in Figure 1a. The sketch in Figure 1b shows the field of view (FOV) of each group. The shaded area is the FOV of the 3D view. Because the targeted objects (organs or tissues) of the collimator are only a short distance from the collimator/detector, the 3D FOV will cover the whole imaged area provided that we can design the collimator/detector slightly longer than the object, other one would use a step-and-scan approach for imaging for entire object.

Comparing to a parallel-hole collimator with the same pixel pitch, the interwoven collimator maintains the same spatial resolution on a plane parallel to the collimator surface [6], while it is able to obtain position information in the third dimension. Since the collimator holes are slanted, gamma-rays travel a slightly longer distance before reaching a hole, going through it and impinging on the detector plane [8]; thus, the sensitivity of the interwoven collimator is lower than a parallel-hole collimator. Their relationship can be roughly estimated by

$$E_{\text{int}erwoven} = E_{parallel} \cdot \sin^2(\alpha) \quad (1)$$

where $E_{\text{int}erwoven}$ and $E_{parallel}$ are the sensitivity of interwoven collimator and parallel-hole collimator respectively, and α is the angle between slanted-hole axis and collimator surface. Because of its lower sensitivity, the interwoven collimator may need a longer image acquisition time depending on the separation of the object of interest and the top surface of the collimator.

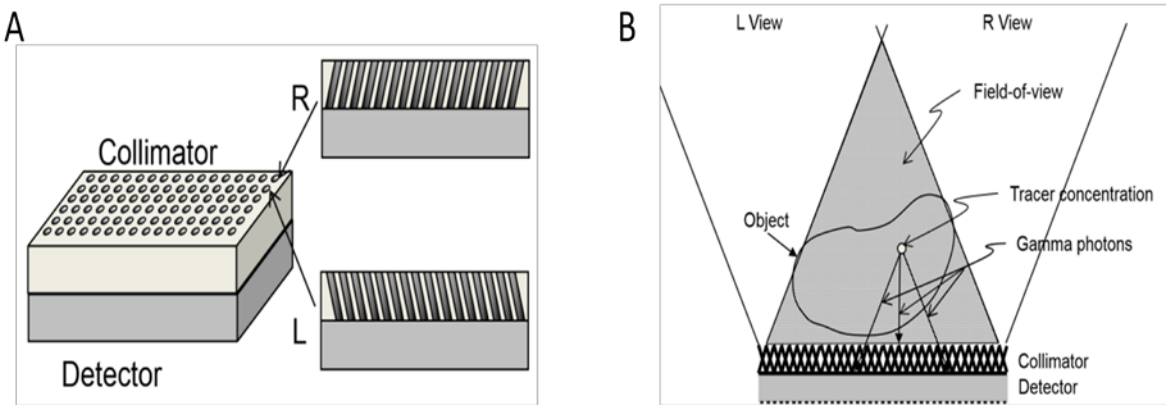

Figure 1. Interwoven collimator. (a) 3D sketch and cross-sectional views of the collimator; and, (b) effective field-of-view of the collimator.

2.2. Geant4 simulation of collimator coupled to pixilated CdZnTe detectors

To verify the imaging capability of the interwoven collimator and study its performance, we carried out Monte Carlo simulations using Geant4 software [7] to estimate the response of the collimator and the detectors to gamma-ray photons. Geant4 is a C++ toolkit for simulating the interaction of particles with matter; it provides a diverse, wide-ranging, yet cohesive set of software components for various detector settings [8]. Each component, ranging from the detector's configuration to the selection of the physics process, and the data output for consequent analysis can be customized at the user end by inheriting the appropriate classes in the toolkit [9]. Table 1 below lists all the components that were defined to simulate the interwoven collimator and the CdZnTe detectors. Table 2 lists the geometries of the interwoven collimator and the CdZnTe detectors that were employed in the ProxiScan gamma camera. Figure 2 illustrates the position and geometries of effective field of view of the simulated interwoven collimator.

We used the code listed in Table 1 to verify the 3D imaging capability of the interwoven collimator for raster scanning and imaging shaped sources.

Table 1. Inherited classes and description.

Defined Class	Inherited Class	Description
MyDetectorBuilder	G4VUserDetectorConstruction	Construct the interwoven collimator and pixilated CdZnTe detectors using the design parameters in Table 2.
MyMaterial	G4Material	Create and register the materials from which the collimator and detector are made—tungsten for the collimator and shielding, and CdZnTe for the detectors.
MyPrimary	G4VUserPrimaryGeneratorAction	Simulate the gamma-rays emitted from a voxel in the 3D FOV. We assumed that the isotope for imaging was ^{99m}Tc. The gamma-rays were emitted in 4π solid angle.
MyPhysicsList	G4VUserPhysicsList	Register all the processes that a low-energy gamma-ray may follow when interacting with the collimator and detectors. The list of processes includes the photoelectric effect (G4LowEnergyPhotoElectric) and Compton scattering (G4LowEnergyCompton).
MyHit	G4VHit	Record the position and deposited energy of interaction points where the primary- or secondary-particles interact with the detector or collimator.
MyDigitizer	G4VDigitizerModule	Calculate the energy deposited in the CdZnTe detector; collect all the hits above a preset threshold and simulate the readout scheme.
MyEventAction	G4VUserEventAction	Process all the hits after the simulation of one primary particle has been completed, and save all the events for all the pixels.

Table 2. Geometries of simulated collimator and detector.

Geometry	Value
Detector volume	16×48×5 mm^3
Detector pixel pitch	1 mm
Collimator thickness	5 mm
Collimator hole diameter	0.5 mm
Slant angle	60º

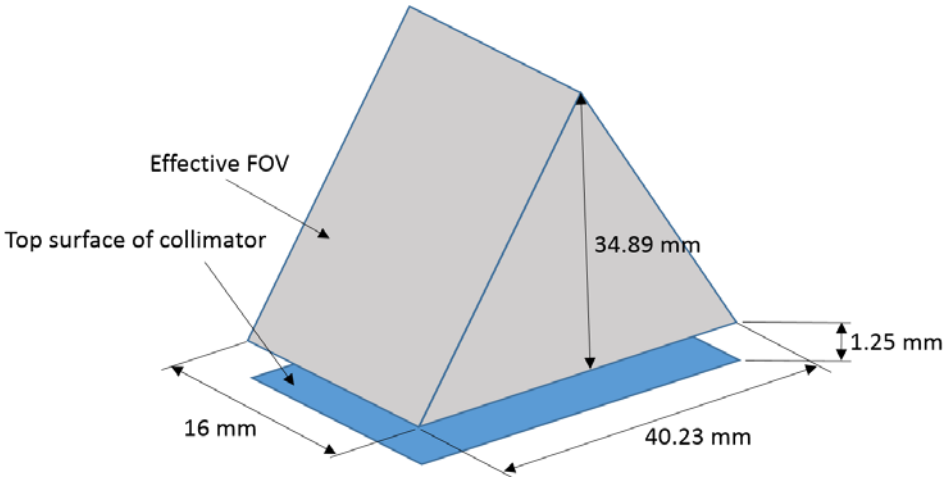

Figure 2. Geometries of the field of view of the simulated interwoven collimator.

Table 3. Specifications of the cluster machine for this research.

Specs	Alpha Group	Beta Group
Quantity	58	32
Model	Dell PowerEdge SC1425	Dell PowerEdge M610 Blades
CPU	(2) Intel Xeon 3.20 GHz	(2) Intel E5530 Quad-core Xeon 2.4 GHz
Memory	2 GB	48 GB
OS	Scientific Linux	Scientific Linux

Raster scan: In this mode, we divided the entire 3D FOV into voxels with dimensions that match the size of the detector pixels (1-mm pitch), and simulated the response of the collimator and detectors to the spherical source in each voxel. The data set generated in this simulation helped us understand the operational principle of the collimator, and were also used to generate the probability matrix for a 3D-image reconstruction (see discussions in next section).

Monte Carlo simulations consume significant CPU time. In this simulation, it averaged 20 minutes to simulate 1,000,000 primary particles emitted from one voxel. For raster scanning with the

geometry configuration in Table 2, there are 14,828 voxels in the entire 3D FOV, and it would take 4,949 hours for a single processor to finish the job. Because the emission of gamma rays from one voxel is independent of that from other voxels, a Linux cluster computer with 488 cores was used to run the simulations in parallel; the task was finished in 36 hours. The specifications of the cluster computer are listed in Table 3.

Shaped-source response: The purpose of this simulation was to collect data on the detector's response to a shaped radioactive source. Here, we modified the class MyPrimary by replacing the single spherical source with (1) multiple spherical sources, or (2) sources with different shapes, e.g. a line source. The data were fed into the image reconstruction algorithm to verify the 3D imaging capability of the interwoven collimator.

2.3. Maximum likelihood expectation maximization

To reconstruct the 3D images from the interwoven collimator, we adapted the maximum likelihood expectation maximization (ML-EM) algorithm [10,11]. The mathematical model of the algorithm is described below for a gamma-camera detector.

Assume $v_i (i = 1,2...n)$ is the activity (unobserved data) in voxel i of the field of view, with the expectation of $\hat{v}_i$, and $d_j (j = 1,2...m)$ is the reading (observed data) of detector pixel j. The goal of ML-EM algorithm is to find $\hat{v}$ that maximizes the likelihood of the observed detector reading d.

Because the gamma-ray emissions of a radioisotope follow a Poisson distribution, the probability of one voxel emitting n_v gamma-ray photons is defined as the following;

$$f(n_v \mid \hat{v}) = P(v = n_v \mid \hat{v}) = e^{-\hat{v}} \frac{\hat{v}^{n_v}}{n_v!} \tag{2}$$

The probability of one emission photon from voxel i being detected by detector pixel j is denoted by p_{ij}, which can be estimated by Monte-Carlo simulation on computer. Apparently, we have $\sum_j p_{ij} \le 1$ as there are always photons that are not captured by the detectors. Then, the expectation of the detector reading is calculated as

$$\hat{d}_j = E(d_j) = \sum_i \hat{v}_i p_{ij} \tag{3}$$

Since it also follows a Poisson distribution, its probability of measuring m_d photons is

$$f(m_d \mid \hat{d}) = P(d = m_d \mid \hat{d}) = e^{-\hat{d}} \frac{\hat{d}^{m_d}}{m_d!}. \quad (4)$$

We define λ_{ij} as the number of photons emitted from voxel i and detected by detector pixel j. Its expectation is

$$\hat{\lambda}_{ij} = \hat{v}_i p_{ij}. \quad (5)$$

We also have

$$\hat{\lambda}_{ij} = \hat{v}_i p_{ij}. \quad (6)$$

Then, the likelihood function is defined as

$$l = \prod_{i,j} e^{-\hat{\lambda}_{ij}} \frac{\hat{\lambda}_{ij}^{\lambda_{ij}}}{\lambda_{ij}!}. \quad (7)$$

The log-likelihood function can be derived as

$$L = \log(l) = \sum_{i,j} \log(e^{-\hat{\lambda}_{ij}} \frac{\hat{\lambda}_{ij}^{\lambda_{ij}}}{\lambda_{ij}!}) = \sum_{i,j} (-\hat{v}_i p_{ij} + \lambda_{ij} \log \hat{v}_i + \lambda_{ij} \log p_{ij} - \log(\lambda_{ij}!)) \quad (8)$$

The ML-EM algorithm has two steps:

1. Expectation step (E step): Calculate the expectation of λ_{ij} using the current estimation of v_i.

$$\lambda_{ij}^{[k+1]} = E(\lambda_{ij} \mid d, v^{[k]}) = \frac{d_j v_i^{[k]} p_{ij}}{\sum_l v_l^{[k]} p_{lj}} \quad (9)$$

2. Maximization step (M step): Calculate the new value of the parameter to maximize the likelihood of the detector's readings using the estimated voxel activity. Apparently, the optimized value of λ is the one that satisfies $\frac{\partial(L)}{\partial v_i} = 0$. Thus,

$$v_i^{[k+1]} = \frac{\sum_j \lambda_{ij}^{[k+1]}}{\sum_j p_{ij}} \tag{10}$$

Combining the two steps, we obtain the final equation for the iteration:

$$v_i^{[k+1]} = \frac{\sum_j \frac{d_j v_i^{[k]} p_{ij}}{\sum_l v_l^{[k]} p_{lj}}}{\sum_j p_{ij}} = \frac{v_i^{[k]}}{\sum_j p_{ij}} \sum_j \frac{d_j p_{ij}}{\sum_l v_l^{[k]} p_{lj}} \tag{11}$$

Algorithm for image reconstruction using the ML-EM method:

1. Initialize $v^{[0]}$ so that $x^{[1]} > 0$.
2. Calculate the estimate of $v^{[k+1]}$ using the following equation:

$$v_i^{[k+1]} = \frac{v_i^{[k]}}{\sum_j p_{ij}} \sum_j \frac{d_j p_{ij}}{\sum_l v_l^{[k]} p_{lj}}$$

3. When the specified accuracy is reached, then stop. Otherwise, repeat step 2.

3. Results

3.1. Raw data - projection images

Figure 3 shows the projection images of a spherical source (D = 0.5 mm) at different heights above the collimator plane with projected position of (0, 0) on the collimator's plane (the X-Y plane). Several conclusions can be drawn from the images that agree with the design concept of this novel collimator:

1. Because of the separation of collimator holes in the interwoven collimator, the projected image of the source also is separated into two groups. As the source moves away from the collimator surface, its two projections are separated further, and the profile of each projection becomes larger. Such enlarged profile is caused by the point spread function as also seen for a parallel-hole collimator.

2. Compared with the 2D projection image of a traditional parallel-hole collimator, each group is an alternatively sampled 2D projection image. Two "half" images are complementary to each other. If we rotate one image by 180º around the middle point of the two images, they will

merge into one 2D-projection image.

3. The centroid of each image can be estimated after interpolation. Let's say, (x_1, y_1) for the top one and (x_2, y_2) for the bottom one. Then, the source location on the X-Y plane can be estimated by

$$x = \frac{x_1 + x_2}{2} \quad \text{and} \quad y = \frac{y_1 + y_2}{2}. \tag{12}$$

Its distance to the collimator plane can be estimated by

$$z = | y_1 - y_2 | \cdot \tan\alpha . \tag{13}$$

Here, α is the slanted angle of the collimator and is less than 90º. The above three equations can be verified easily from the images in Figure 3.

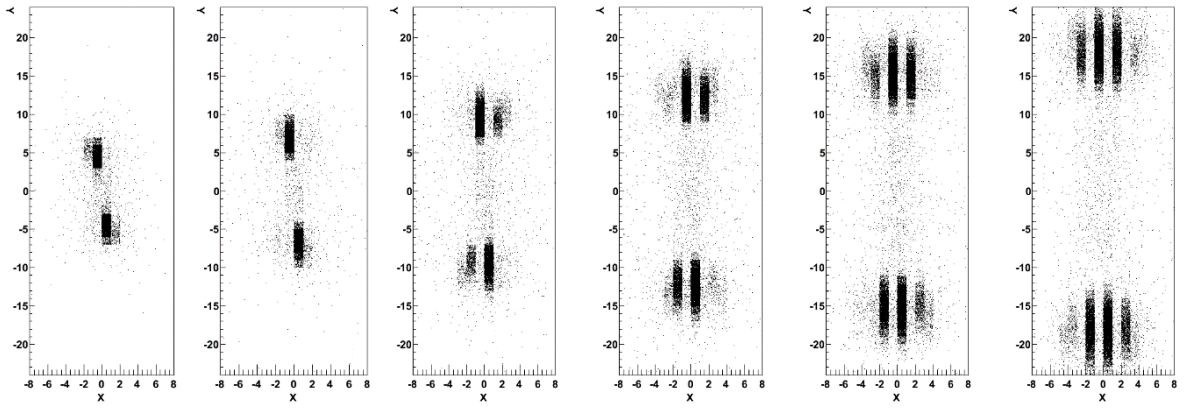

(a) (b) (c) (d) (e) (f)

Figure 3. (a)–(f) projection images of a spherical source at a vertical distance to the collimator plane of 6, 10, 15, 20, 25 and 30 mm.

3.2. Reconstruction of a 3D image from the interwoven collimator

To test the ML-EM algorithm, a simple phantom with 8 spherical sources was built, and the response of the collimator plus detectors was simulated in Geant4. Each spherical source is 0.5 mm in diameter, and located at one vertex of a 5-mm sized cube. The projection image of the phantom from the Geant4 simulation was fed into the ML-EM algorithm; Figure 4 shows the reconstructed image of the phantom. The center of the cube is located at (0, 0, 11) in the coordination system. Certainly, all the 8 spherical sources are resolved clearly. Their positions agree with those of the phantom. The top 4 sources had more background signals because they were further from the detector plan, and because of the limited number of views obtained.

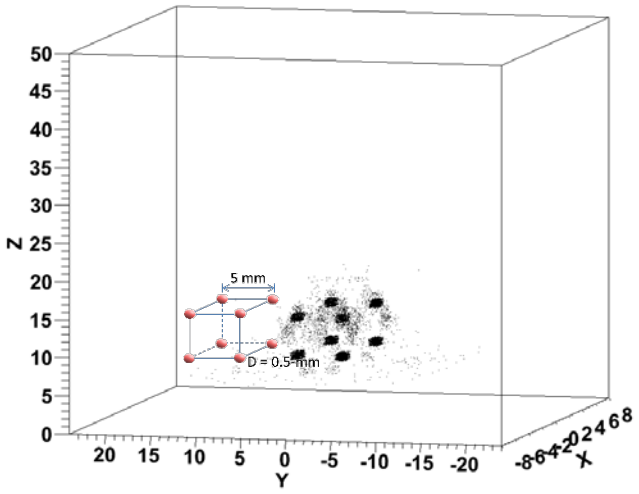

Figure 4. Reconstructed image of 8 spherical sources that were located at the vertices of a cube.

4. Discussion and Conclusions

We developed a novel collimator that targets specific applications in nuclear-medical imaging wherein the operational space is extremely constrained and rotation around the object of interest is not anatomically possible, such as in trans-rectal prostate imaging. To construct 3D images using the collimator, the ML-EM algorithm was adapted successfully.

After we demonstrate the concept of an interwoven collimator for 3D imaging using point sources in a laboratory setting, our next step is to implement this technique in a next-generation endocavity gamma camera designed for clinical measurements. Detailed engineering designs are being carried out as part of this development effort. We will report the test results from this new compact gamma camera in a subsequent manuscript.

Acknowledgments

The CdZnTe detector R&D was supported by the U.S. Department of Energy's Office of Nonproliferation Research and Development. The ProxiScan R&D and engineering work was supported by Hybridyne Imaging Technologies, Inc. The manuscript has been authored by Brookhaven Science Associates, LLC under Contract no. DE-AC02-98CH1-886.

Conflict of Interest

All authors declare no conflicts of interest in this paper.

References

1. Mariani G, Bruselli L, Kuwert T, et al. (2010) A review on the clinical uses of SPECT/CT. *Eur J Nucl Med Mol Imaging.* DOI: 10.1007/s00259-010-1390-8.
2. Cui Y, Lall T, Tsui B, et al. (2011) Compact CdZnTe-based gamma camera for prostate cancer imaging. *Proc SPIE 8192, International Symposium on Photoelectronic Detection and Imaging 2011*, 919255. doi:10.1117/12.901078.
3. American Cancer Society, https://www.cancer.org.
4. Turkbey B, Pinto PA, Choyke PL (2009) Imaging techniques for prostate cancer: Implications for focal therapy. *Nat Rev Urol* 6: 191-203. Doi:10.1038/nrurol.2009.27.
5. Turkbey B, Albert PS, Kurdziel K, et al. (2009) Imaging localized prostate cancer: Current approaches and new developments. *Am J Roentgenology* 192: 1471-1480.
6. Moore RH, Alpert NM, Strauss HW (1983) A Variable Angle Slant-Hole Collimator. *J Nucl Med* 24: 61-65.
7. Geant4 official website: http://geant4.cern.ch.
8. Agostinelli S, Allison J, Amado K, et al. (2003) Geant4—a simulation toolkit. *Nucl Instrum Methods* 506: 250-303.
9. Allison J, Amako K, Apostolakis J, et al. (2006) Geant4 Developments and Applications. *IEEE Trans Nucl Sci* 53: 270-278.
10. Moon TK (1996) The expectation-maximization algorithm. *IEEE Signal Processing Magazine* 13: 47-60.
11. Barrett H, Hunter W, Miller B, et al. (2009) Maximum-likelihood methods for processing signals from gamma-ray detectors. *IEEE Trans Nucl Sci* 56: 725-735.

AIMS Press